Article

Mechanical Responses of Ductile Aluminum Alloy under Biaxial Non-Proportional Tensile Reverse Loading Patterns

Zhichao Wei * , Steffen Gerke and Michael Brünig

Institut für Mechanik und Statik, Universität der Bundeswehr München, Werner-Heisenberg-Weg 39, D-85577 Neubiberg, Germany; steffen.gerke@unibw.de (S.G.); michael.bruenig@unibw.de (M.B.)
* Correspondence: zhichao.wei@unibw.de; Tel.: +49-89-6004-3413

Abstract: This paper deals with the study of the mechanical responses of ductile metals under biaxial non-proportional cyclic loading tests. The biaxially loaded HC specimens manufactured from 4 mm thick aluminum alloy sheets (EN AW 6082-T6) are subjected to various loading paths, including monotonic and cyclic loading conditions. The aim is to investigate the plastic, damage, and fracture behavior of the material under these different loading scenarios. In terms of numerical aspects, a modified anisotropic two-surface cyclic plastic–damage continuum model is used to predict the material behavior in the load-displacement field and different strain fields. Numerically predicted stress states are analyzed in detail to gain a better understanding of the damage mechanisms. Moreover, the scanning electronic microscopy (SEM) pictures taken from the fracture surfaces confirm the dependency of the damage mechanisms on the loading histories. The present work indicates the importance of considering different loading conditions for the accurate prediction of material responses.

Keywords: ductile damage and fracture; non-proportional experiments; reverse loading; numerical simulations

1. Introduction

Engineering structures and manufacturing processes often experience complex loading conditions, such as non-proportional and cyclic loadings. Thus, it is essential to understand the mechanical response of the material under various loading cases. One of the main tasks is to accurately predict the plastic, damage, and fracture behavior. In the last decades, a large body of literature has indicated that the damage and fracture behavior depends on the stress states [1–6]. However, most researchers focus on monotonic or uniaxial cyclic loading conditions [7–13]. It is evident that reverse loading histories significantly alter ductile plastic, damage, and fracture behavior [12,14–17]. However, their studies were not able to cover a wide range of stress triaxialities, limiting their ability to calibrate the stress-dependent continuum theory under a wide range of stress triaxiality. In this context, biaxial tests were conducted to satisfy the above-mentioned requirements. Proportional and non-proportional biaxial loading experiments have been widely discussed in the literature [18–21]. Although a wide range of stress states has been successfully generated, the literature still needs to discuss the reverse loading effect under multi-axial stress states. Moreover, a change in the loading path, such as tension to shear or shear to tension, can significantly change the ductility of the metals. For example, the ductility of the aluminum alloy EN AW 6082-T6 [22,23] and the aluminum alloy 2198 [13,21] reduces under load path change from pre-shear to tension. On the other hand, various preloads (pre-tension, pre-compression, or pre-shear) significantly affect the strain-to-fracture behavior under non-proportional loading [18]. Therefore, a set of biaxially loaded non-proportional reverse loading experiments is newly designed for the present work to cover a wide range of stress triaxialities. The damage and fracture behavior in non-proportional biaxial shear reverse experiments has been extensively discussed in previous work by [22]. In this paper, the focus is on non-proportional biaxial tensile reverse (tension-compression) experiments. In the experiments, the shear preload is first imposed on the specimen, resulting

in pre-damage in the investigated aluminum alloy EN AW 6082-T6. Subsequently, the shear preload remains constant, and the monotonic and cyclic tensile loads are superimposed on the specimens. It is worth noting that conducting experiments with compressive loading on metal sheets presents a significant challenge in avoiding buckling [24,25]. Most recently, a newly designed downholder has been employed to apply compressive loads to a thin metal sheet with a thickness of only 1 mm. Therefore, the same downholder and experimental technique have also been utilized in the present work. Moreover, the digital image correlation (DIC) technique monitors the changes in force and displacement fields and corresponding strain fields during the experiments. Scanning electron microscopy images taken from the fracture surfaces are provided to elucidate and comprehend the damage and failure mechanisms.

Concerning the material modeling, the classic Gurson model incorporates the softening into the plastic yield condition and the change in the porosity concerning the volume change in the plastic strain [26]. This classic model is not suitable for simulating the shear failure under nearly zero stress states. Even though the Gurson model has been extensively modified to overcome the mentioned shortcomings [27–32], it could not accurately characterize the anisotropy of the damage and fracture behavior. Hence, several anisotropic continuum damage models are proposed to capture the anisotropic characteristics [33–40]. Typically, Brünig [35] and Brünig et al. [41] introduced a novel anisotropic damage strain rate tensor into the proposed constitutive model to predict the different damage mechanisms under varying stress states. In addition, Wei et al. [22] extended the Brünig anisotropic plastic–damage model by considering the combined plastic hardening and softening damage rule to simulate the material behavior under cyclic loading conditions.

In the present work, an anisotropic two-surface cyclic elastic–plastic–damage continuum model [22] is utilized to predict material behavior at both macro- and micro-levels. A noteworthy aspect of the present work is the design of newly designed non-proportional biaxial tensile reverse experiments with 4 mm metal sheets, which are employed to investigate damage and fracture behavior. This paper is structured as follows: The proposed material model is briefly summarized in Section 2. Then, in Section 3, the experimental settings, geometry, and loading paths are discussed in detail. After that, the experimental and numerical results, including load-displacement fields, strain fields, and corresponding stress state and damage mechanisms, are presented in Section 4. Some important conclusions are drawn in Section 5.

2. Constitutive Theory

This section briefly discusses the proposed anisotropic cyclic plastic–damage continuum model incorporating combined hardening and softening rules; see [12,22,35] for more details.

2.1. Plastic Yield Criterion with Combined Hardening

The stress differential (SD) effect is a widely observed phenomenon in ductile metals [12,42,43] and geomaterials [44]. Additionally, the Bauschinger effect is also noticeable under cyclic loading for ductile metals. Hence, the Drucker–Prager yield criterion considering the combined hardening law

$$f^{\mathrm{pl}} = \sqrt{\frac{1}{2}\mathrm{dev}(\bar{\mathbf{T}} - \bar{\boldsymbol{\alpha}})\cdot\mathrm{dev}(\bar{\mathbf{T}} - \bar{\boldsymbol{\alpha}})} - \bar{c}(1 - \frac{a}{\bar{c}}\,\mathrm{tr}(\bar{\mathbf{T}} - \bar{\boldsymbol{\alpha}})) = \sqrt{\bar{J}_2} - \bar{c}(1 - \frac{a}{\bar{c}}\bar{I}_1) = 0 \quad (1)$$

is used to characterize the plastic behavior under monotonic and cyclic loading conditions, where $\bar{\mathbf{T}}$ and $\bar{\boldsymbol{\alpha}}$ are the effective stress tensor and the effective back stress tensor, respectively, and $\bar{I}_1$ and $\bar{J}_2$ are the first and second deviatoric effective stress invariants. The current equivalent effective yield stress is denoted as $\bar{c}$, and the hydrostatic coefficient $\frac{a}{\bar{c}}$ accounts for the SD effect.

The plastic strain rate tensor is defined as the derivative of the plastic potential function g^{pl} with respect to the reduced effective stress tensor $(\bar{\mathbf{T}} - \bar{\boldsymbol{\alpha}})$

$$\dot{\mathbf{H}}^{\mathrm{pl}} = \dot{\lambda}\frac{\partial g^{\mathrm{pl}}(\bar{\mathbf{T}} - \bar{\boldsymbol{\alpha}})}{\partial(\bar{\mathbf{T}} - \bar{\boldsymbol{\alpha}})} = \dot{\lambda}\frac{1}{2\sqrt{\bar{J}_2}}\,\mathrm{dev}(\bar{\mathbf{T}} - \bar{\boldsymbol{\alpha}}) = \dot{\gamma}\bar{\mathbf{N}}, \quad (2)$$

where the equivalent plastic strain rate $\dot{\gamma}$ is equal to $\frac{1}{\sqrt{2}}$ times the non-negative plastic multiplier $\dot{\lambda}$, and $\bar{\mathbf{N}}$ denotes the deviatoric normalized plastic strain flow direction.

The non-linear Voce strain hardening law is given by

$$\bar{c} = c_0 + Q_1(1 - e^{-p_1\gamma}) + Q_2\xi(1 - e^{-p_2\gamma}) \tag{3}$$

with the material constants c_0, Q_1, Q_2, p_1, and p_2 determined from the uniaxial tensile test, the equivalent plastic strain γ, and the stress state-dependent function ξ; see [12,22] for more details.

Moreover, the modified Chaboche non-linear kinematic hardening [9,12,45] taking into account three decomposed rates of the effective back stress terms $\dot{\bar{\boldsymbol{\alpha}}}$ is expressed as

$$\dot{\bar{\boldsymbol{\alpha}}} = \dot{\bar{\boldsymbol{\alpha}}}_1 + \dot{\bar{\boldsymbol{\alpha}}}_2 + \dot{\bar{\boldsymbol{\alpha}}}_3 , \tag{4}$$

with

$$
\begin{aligned}
\dot{\bar{\boldsymbol{\alpha}}}_1 &= b_1\chi\dot{\mathbf{H}}^{\mathrm{pl}} - b_2\chi\dot{\gamma}\bar{\boldsymbol{\alpha}}_1 , \\
\dot{\bar{\boldsymbol{\alpha}}}_2 &= b_3\dot{\mathbf{H}}^{\mathrm{pl}} - b_4\dot{\gamma}\bar{\boldsymbol{\alpha}}_2 , \\
\dot{\bar{\boldsymbol{\alpha}}}_3 &= b_5\dot{\mathbf{H}}^{\mathrm{pl}} - (1 - \cos^2\theta)b_6\dot{\gamma}\bar{\boldsymbol{\alpha}}_3 ,
\end{aligned}
\tag{5}
$$

where $b_1 \ldots b_6$ are material parameters calibrated by the uniaxial monotonic and cyclic tests, $\chi = 0.8e^{-300\gamma} + 0.2$ represents an non-linear Decay function [12], and the angle θ characterizes the direction between the effective reduced stress tensor $(\bar{\mathbf{T}} - \bar{\boldsymbol{\alpha}})$ and the rate of the third effective back stress tensor $\dot{\bar{\boldsymbol{\alpha}}}_3$.

In addition, a scalar isotropic hardening ratio ρ_h is introduced to combine the isotropic hardening part $(\mathring{c})$ and the kinematic hardening part $(\mathring{\alpha})$ in the form

$$\dot{\sigma} = k_h\rho_h\mathring{c} + (1 - k_h\rho_h)\mathring{\alpha} , \tag{6}$$

where $\dot{\sigma}$ denotes the current total hardening rate, and k_h describes the change in the hardening rate after reverse loading [22].

2.2. Damage Condition with Combined Softening

The modified stress state-dependent anisotropic damage condition considering the combined softening rule is given by

$$f^{\mathrm{da}} = \hat{\alpha}\,\mathrm{tr}(\mathbf{T} - \boldsymbol{\alpha}) + \hat{\beta}\sqrt{\frac{1}{2}\mathrm{dev}(\mathbf{T} - \boldsymbol{\alpha})\cdot\mathrm{dev}(\mathbf{T} - \boldsymbol{\alpha})} - \tilde{\sigma} = \hat{\alpha}I_1 + \hat{\beta}\sqrt{J_2} - \tilde{\sigma} = 0 , \tag{7}$$

where $\mathbf{T}$ is the Kirchhoff stress tensor, $\boldsymbol{\alpha}$ denotes the damage back stress tensor, $\tilde{\sigma}$ represents the current equivalent softening damage stress, and I_1 and J_2 are stress invariants. In addition, the stress state-dependent coefficients $\hat{\alpha}$ and $\hat{\beta}$ have different effects on the onset of damage, and these parameters can be identified from micro-mechanical studies [22,41]. Moreover, the formulas for $\hat{\alpha}$ and $\hat{\beta}$ are thoroughly discussed in [22].

Furthermore, the damage strain rate tensor

$$\dot{\mathbf{H}}^{\mathrm{da}} = \dot{\mu}(\tilde{\alpha}\frac{1}{\sqrt{3}}\mathbf{1} + \tilde{\beta}\tilde{\mathbf{N}}) \tag{8}$$

characterizes the evolution of macroscopic irreversible strains caused by damage processes acting on the micro-level, where $\dot{\mu}$ is a non-negative damage multiplier, and $\tilde{\alpha}$ and $\tilde{\beta}$ depend on the stress states. The formulas and identifications of $\tilde{\alpha}$ and $\tilde{\beta}$ can be found in [22,41].

In addition, the non-linear isotropic softening law based on the equivalent damage strain μ is formulated as

$$\tilde{\sigma} = \tilde{\sigma}_0 - C_1 e^{-C_2\mu} \tag{9}$$

where $\tilde{\sigma}_0$ denotes the initial damage stress, and C_1 and C_2 are material constants.

Moreover, the damage strain rate tensor $\dot{\mathbf{H}}^{\mathrm{da}}$ is introduced in the formulation of the kinematic softening law

$$\dot{\boldsymbol{\alpha}} = d_1 \dot{\mathbf{H}}^{\mathrm{da}} - d_2 \dot{\mu} \boldsymbol{\alpha} \tag{10}$$

to characterize the transformation of the damage surface under various loading cases, where d_1 and d_2 are material constants.

Similar to the hardening ratio ρ_h, the softening ratio ρ_s is proposed to combine the isotropic part $\dot{\tilde{\sigma}}$ and kinematic part $\dot{\alpha}_{\mathrm{eq}}$

$$\dot{\sigma} = \rho_s \dot{\tilde{\sigma}} + (1 - \rho_s) \dot{\alpha}_{\mathrm{eq}} . \tag{11}$$

The softening ratio ρ_s is set in the current study to be the same as the hardening ratio ρ_h.

3. Experimentation

3.1. Material and the HC Specimen

In this study, the investigated material is the aluminum-magnesium-silicon (Al-SiMgMn) alloy EN AW 6082-T6, which is a medium strength alloy. Table 1 shows the composition of this aluminum alloy. Moreover, the Young's modulus is measured as $E = 69,000$ MPa, and the Poisson's ratio is $\nu = 0.29$.

Table 1. Composition of EN-AW 6082-T6.

Al	Si	Mg	Mn	Fe	Cu	Zn	Ti	Others
97.29%	0.90%	0.70%	0.47%	0.37%	0.09%	0.09%	0.03%	0.06%

The geometry of the HC specimen is shown in Figure 1. There are four 2 mm (Figure 1a,b) thick notches in the center of the HC specimen, where stresses and strains are expected to localize, leading to fracture. The distances of the central notch part are 8 mm in the direction of axis 1 and 32 mm in the direction of axis 2, respectively, enabling cyclic loading in both axes. For the load-displacement analysis, the force and the relative displacement are defined as

$$F_i = \frac{F_{i,1} + F_{i,2}}{2}, \quad \text{and} \quad \Delta u_{ref} = u_{i.1} + u_{i.2} , \tag{12}$$
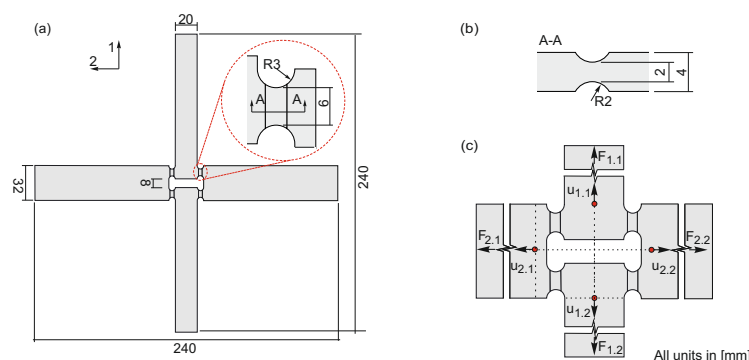
respectively; see Figure 1c.

Figure 1. HC–specimen geometry: (**a**) overview of the HC-specimen and a detailed view of the notched part, (**b**) cross-section A-A of the HC-specimen, and (**c**) measurement points and loads in axis 1 and axis 2.

3.2. Biaxially Loaded Non-Proportional Monotonic and Cyclic Tests

The experiments were conducted on the electromechanical biaxial planar testing machine LFM-BIAX 20 kN provided by Walter + Bai, Switzerland. All tests were per-

formed under quasi-static loading conditions, maintaining a consistent machine velocity of 0.04 mm/min during the experiments. The digital image correlation (DIC) technique, including the lighting system (LED lights type FL-B50 and type FL-B25) and cameras (6 MPx mounting 75 mm lenses), as shown in Figure 2a, was used to monitor the changes in forces and displacements, and the region of interest (ROI) was set to be approximately 2700 Px × 2200 Px in the center of the HC specimen. The average resolution at the center of the HC specimen is approximately 56 Px/mm, with a subset (facet size) of 33 Px and a selected grid spacing (overlap) of 11 Px. In addition, the newly designed downholder (see Figure 2c,d) prevents buckling during the cyclic compressive loading. After specimen failure, the representative fracture surfaces were selected to examine using the scanning electric microscope (SEM) equipped with the lanthanum hexaboride electron emitter (LaB_6) and the Everhart–Thornley (ET) detector to verify the damage and fracture behavior.
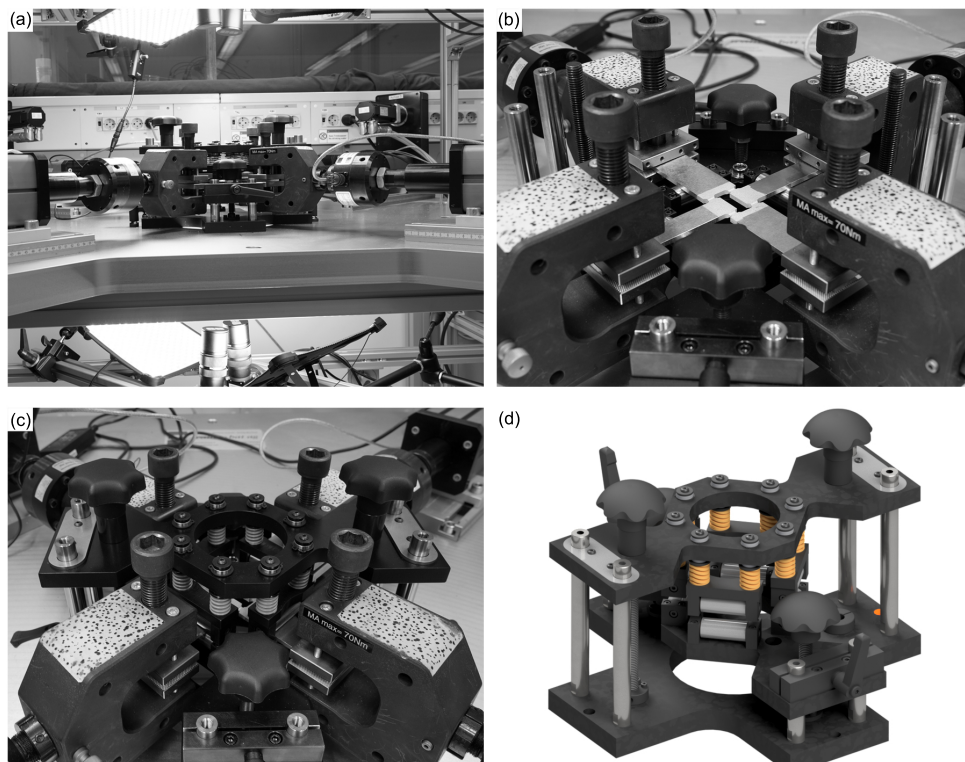

Figure 2. Biaxial testing machine and experimental settings: (**a**) lighting system and cameras, (**b**) clamping and specimen, and (**c**,**d**) downholder.

During the experiments, the monotonic tensile test (mon-S0) and associated cyclic test (cyc-S0) are performed to generate a high stress triaxiality ($\eta > \frac{1}{3}$). The symbol S0 means the monotonic (mon) or cyclic (cyc) loads are subjected to axis 2 superimposed by 0 kN on axis 1; for axes coordinate, see Figure 3. In addition, the mon-S5.5 and cyc-S5.5 experiments are specifically designed to investigate the influence of a preload of 5.5 kN on axis 1 on the material response, without unloading until failure. Furthermore, this study includes tension–compression–tension (TCT) and compression–tension (CT) cyclic loading patterns superimposed on axis 2. The experiments are referred to as cyc-S5.5-TCT and cyc-S5.5-CT, respectively. Moreover, two different tension–compression–tension (TCT) tests, differing in compressive loading paths, are designed to study the effect of compressive loads on material behavior.
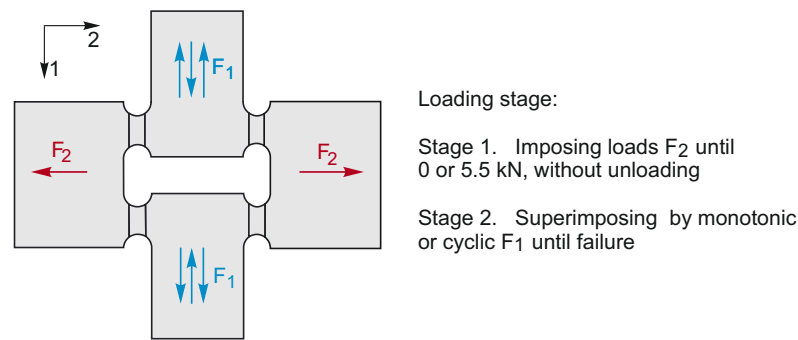
Figure 3. Loading paths.

4. Model Validation

4.1. Material Parameter Calibration

The material parameters can be categorized into elastic (Table 2), plastic (Table 3), and damage (Table 4) parameters. The elastic and plastic parameters are calibrated by the uniaxial monotonic and cyclic tests. On the other hand, the damage softening parameters are identified from micro-simulations. The detail of parameter identification has been discussed in [12,22]. It is worth noting that the initial yield stress $c_0 = 150$ MPa in this study is set to be higher than in previous numerical simulations ($c_0 = 139$ MPa) due to changes in the specimen manufacturing processes. Thus, the initial equivalent damage stress is also newly inversely determined as $\tilde{\sigma}_0 = 320$ MPa.

Table 2. Elastic parameters.

E [MPa]	ν [-]
69,000	0.29

Table 3. Plastic parameters.

c_0 [MPa]	Q_1 [MPa]	Q_2 [MPa]	p_1 [-]	p_2 [-]	b_1 [MPa]	b_2 [-]	b_3 [MPa]
150	74.93	21.32	8.96	676.01	61,250	1750	895

b_4 [-]	b_5 [MPa]	b_6 [-]	$a/\bar{c}$ [TPa^{-1}]	ρ_h			
15	125	7.5	32	0.41			

Table 4. Damage parameters.

$\tilde{\sigma}_0$ [MPa]	C_1 [MPa]	C_2 [-]	d_1 [MPa]	d_2 [-]	$\eta_1 \ldots \eta_4$ [MPa]	ρ_s
320	0.004207	92.97	-0.51	-84	$-10,000$	0.41

4.2. Mesh and Boundary Conditions

The detailed numerical implementation of the proposed material model is discussed in [23], and it has been successfully implemented as a user-defined subroutine in Ansys.

A quarter of the HC specimen with 22,502 solid185 elements is analyzed during the numerical stimulation due to the symmetry of the HC specimen; see Figure 4a. A mesh refinement (0.25 mm × 0.125 mm × 0.1 mm along axes 1, 2, and 3) is taken into account in the notched region where the damage strain is localized, as depicted in Figure 4b. It is worth noting that the used element dimensions are determined by comparing the results of the strain localization distribution obtained from the FE simulation with the ones from the DIC. For the boundary conditions, the symmetric boundary conditions are imposed on the

symmetric surfaces. Initially, the displacements are first applied only to axis 1 to achieve the target forces (0 kN or 5.5 kN). Subsequently, the displacements are removed from axis 1 and imposed on the associated forces (0 kN or 5.5 kN), while displ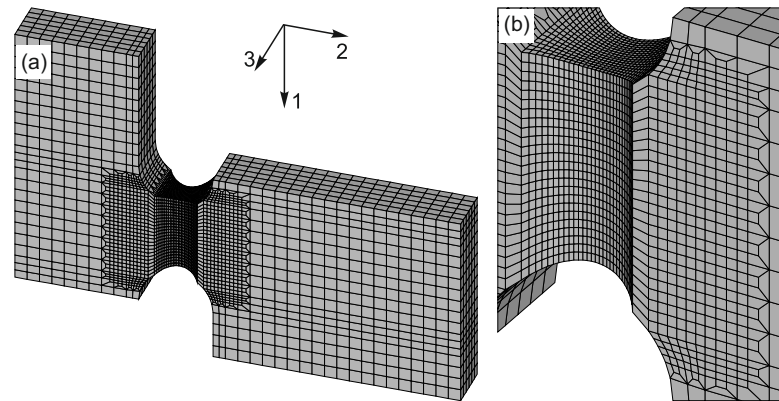acements are simultaneously applied to axis 2. Subsequently, the displacements are removed from axis 1 and imposed on the associated forces (0 kN or 5.5 kN), while displacements are simultaneously applied to axis 2.

Figure 4. Mesh: (**a**) quarter of the HC specimen; (**b**) notched region.

5. Experimental Results and Numerical Simulations

In this section, the comparison between experimental and numerical results is discussed in three different aspects: load-displacement fields, strain fields, stress state, and damage mechanisms.

5.1. Global Fields: Load-Displacement Behavior

Figure 5 shows the global load-displacement curves for the monotonic and cyclic tensile loading tests.

The numerical results agree well with the experimental ones in both axes. In the case of the experiments with preloads, the experimental fracture forces in axis 2, $F_2^{\text{fr,exp}}$, are 10.71 kN and 11.01 kN, respectively. The experimental fracture displacement is $\Delta u_2^{\text{fr,exp}}$ from the zero force at the last tensile loading pattern to the fracture point (FP). Thus, the fracture displacements for the mon-S0 and cyc-S0 experiments are 0.42 mm and 0.31 mm, respectively.

In the case of experiments superimposed by 5.5 kN (Figure 5c), the fracture forces in axis 2, F_2^{fr}, under cyclic loading conditions significantly differ from the monotonic test (mon-S5.5). The mon-S5.5 test fails at the fracture displacement $\Delta u_2^{\text{fr,exp}} = 0.07$ mm with the fracture force $F_2^{\text{fr,exp}} = 3.66$ kN. Clearly, the specimen breaks quickly after the tensile load is imposed on axis 2. As shown in Figure 5d, the cyc-S5.5-CT fracture occurs at $\Delta u_2^{\text{fr,exp}} = 0.13$ mm, and the fracture force reaches $F_2^{\text{fr,exp}} = 6.62$ kN. Moreover, the cyclic loading patterns cyc-S5.5-TCT-A and cyc-S5.5-TCT-B are firstly subjected to the same machine displacements in the first tensile loading path (T), and then, different degrees of compressive machine displacements are imposed during the second loading path (C); see Figure 5e,f. The fracture force $F_2^{\text{fr,exp}} = 5.52$ kN for the cyc-S5.5-TCT-A is smaller than that of the cyc-S5.5-TCT-B test ($F_2^{\text{fr,exp}} = 6.71$ kN). In addition, the fracture displacements are $\Delta u_2^{\text{fr,exp}} = 0.09$ mm and 0.12 mm for the the cyc-S5.5-TCT-A and cyc-S5.5-TCT-B tests, respectively.
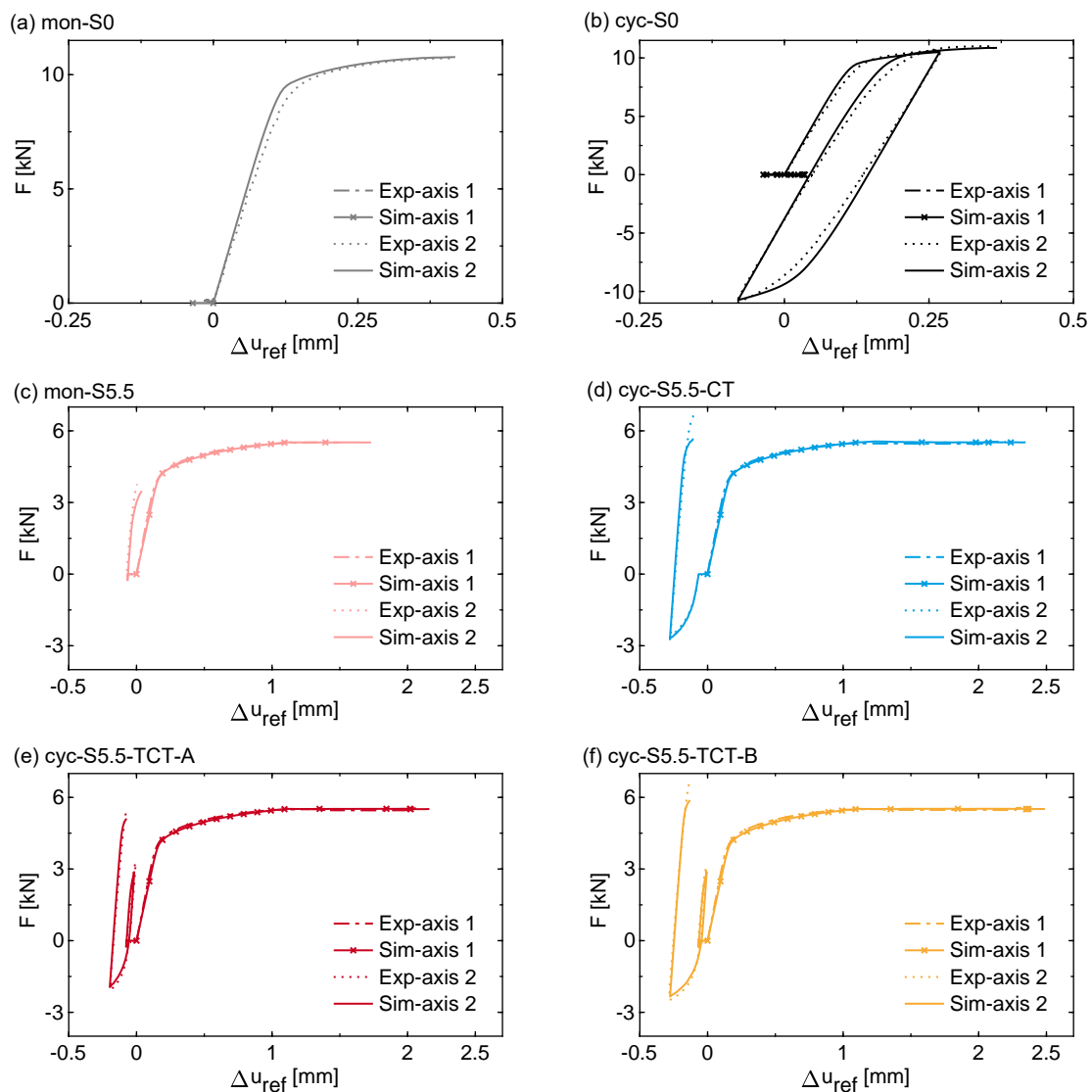
Figure 5. Experimental and numerical load-displacement curves for different monotonic and cyclic loading patterns.

Furthermore, the cyc-S5.5-CT and cyc-S5.5-TCT-B experiments have similar relative compressive displacements $\Delta u_2^{\text{com,exp}} = 0.21$ mm, as shown in Figure 5d,f. Most interestingly, the fracture forces $\Delta u_2^{\text{fr,exp}}$ and displacements $F_2^{\text{fr,exp}}$ show no apparent difference between the cyc-S5.5-CT and cyc-S5.5-TCT-B experiments. Moreover, as mentioned above, there is a significant difference in fracture forces between the cyc-S5.5-TCT-A and cyc-S5.5-TCT-B tests. These findings indicate that the compressive loading pattern (C) significantly influences the fracture behavior compared to the first tensile loading pattern. Furthermore, it is clear that the loading histories and preloads obviously affect the mechanical response of the investigated aluminum alloy.

5.2. Local Fields: Total Strain and Damage Strain

The digital image correlation (DIC) technique monitors and analyzes the total strain fields in the experiments.

The experimental distributions of the total stains A_1 on the notch surfaces obtained from DIC are shown in Figure 6. In addition, the numerically predicted first principal strains A_1 are also illustrated in Figure 6 to be compared with the experimental results. Obviously, the numerical results agree well with the experimental ones. The maximum first

principal strains A_1 are 0.11 and 0.10 for the mon-S0 and cyc-S0 experiments, respectively. In both cases, the first principal strains distribute as an ellipse on the notch surfaces.
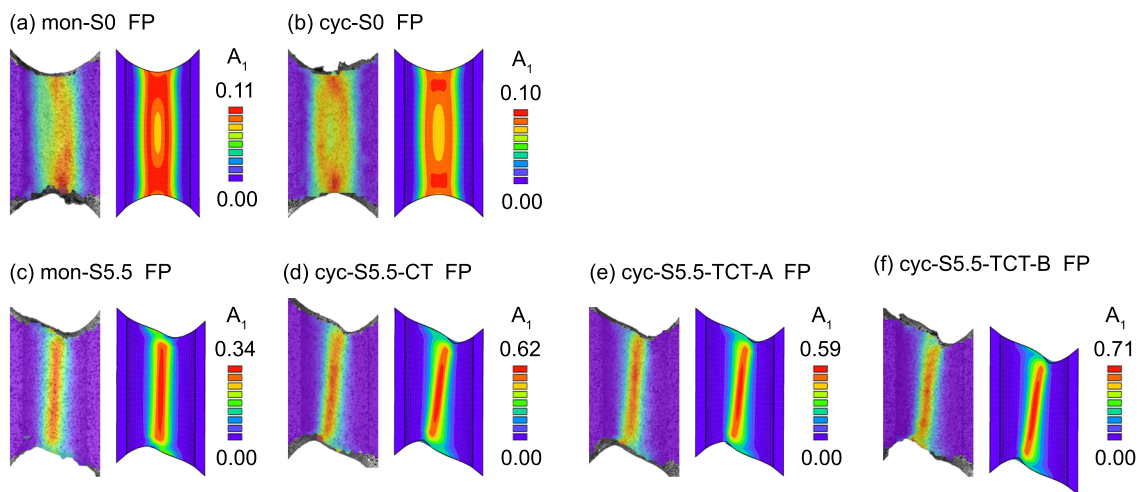

Figure 6. Experimental and numerically predicted distribution of the first principal strains A_1 on the notch surfaces (FP= fracture point).

Figure 6c shows the distribution of the first principal total strain A_1 as a shear band with a maximum value of 0.34 at the center of the notch surface. On the other hand, the shapes and angles of the shear bands in the distributions of the cyc-S5.5-CT, cyc-S5.5-TCT-A, and cyc-S5.5-TCT-B tests show no apparent difference, but the maximum values differ from each other; see Figure 6d,f. Among them, the cyc-S5.5-TCT-B experiment has the maximum first principal strain $A_1 = 0.71$. The maximum values of the first principal strain are 0.62 and 0.59 undergoing the cyc-S5.5-CT and cyc-S5.5-TCT-A loading paths, respectively.

Furthermore, the strain-displacement curves are additionally plotted in Figure 7 to characterize the changes in the first principal strains A_1 during the loading processes. It is worth noting that the experimental and numerical data are average values obtained within a region of interest (ROI) with an area of 0.25 mm × 0.50 mm at the center of the notch surfaces. The numerical and experimental results exhibit good agreement with respect to both quantitative values and evolutionary trends. Moreover, the evolution paths of the first principal strain vary under different loading conditions. This indicates the influence of loading histories and preloads on the plastic behavior.

In the proposed theory, the damage strain tensor $\mathbf{A}^{\mathrm{da}}$ characterizes the volume changes and shape deformation of the micro-defects. Moreover, the localization of the damage strain $\mathbf{A}^{\mathrm{da}}$ might predict the occurrence and location of the fracture. Therefore, the distributions of the first principal damage strains A_1^{da} are illustrated in Figure 8. There is no damage numerically predicted on the notch surfaces for the mon-S0 and cyc-S0 tests, but the damage strains A_1^{da} are highly localized as an ellipse on the notched cross-sections with maximum values of 2.47% and 1.82%, respectively. Moreover, this trend is consistent with the distributions of the first principal strains A_1 for the mon-S0 and cyc-S0 experiments, where the maximum principal strain for the mon-S0 test is larger than that of the one under cyc-S0 loading conditions. On the other hand, the localization of the damage strain A_1^{da} on the center of the notched cross-sections confirms that the fracture behavior first occurs in the middle of the specimen and then spreads outward, similar to what is observed in the uniaxial tension tests [12].
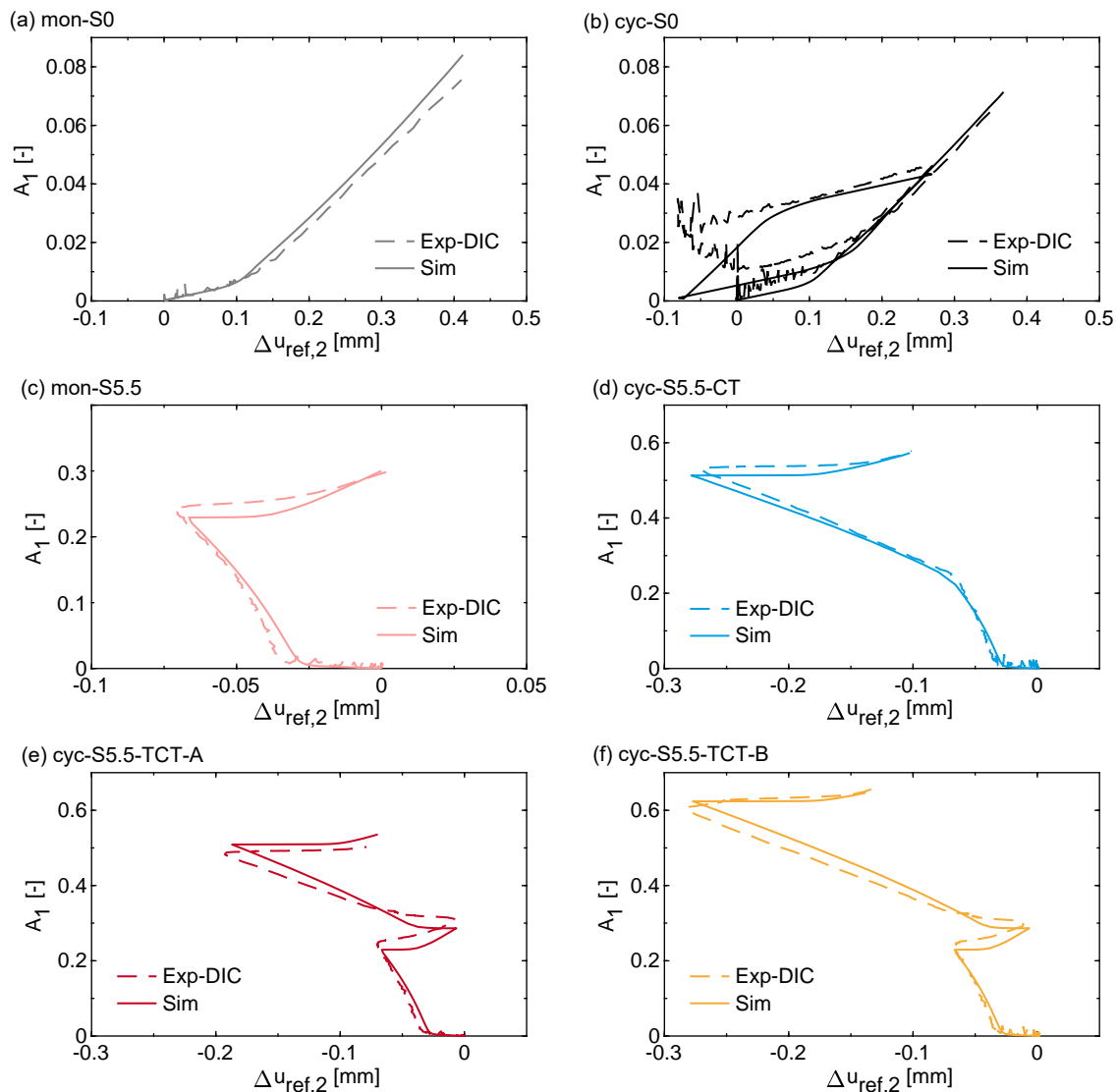
Figure 7. Experimental and numerical strain-displacement curves.

In the experiments superimposed by 5.5 kN, varying maximum first principal damage strains A_1^{da} are observed on the notch surfaces. The mon-S5.5 test has the smallest maximum damage strain $A_1^{da} = 0.15\%$ and the smallest principal total strain; see Figures 6c and 8c. In contrast to the total strain in cyclic loading cases, the cyc-S5.5-CT loading pattern predicts the largest maximum principal damage strain $A_1^{da} = 1.83\%$. In the case of the cyc-S5.5-TCT loading patterns, numerical predictions show damage appearing as shear bands on the notch surfaces and butterfly-shaped patterns on the notched cross-sections. Moreover, $A_1^{da} = 1.72\%$ for the cyc-S5.5-TCT-B, which is slightly larger than that of the cyc-S5.5-TCT-A test ($A_1^{da} = 1.68\%$). These findings indicate that the monotonic and cyclic loading conditions and the degree of preloads significantly change the material matrix, i.e., the shape and volume of the micro-defects, resulting in different damage and fracture behavior.
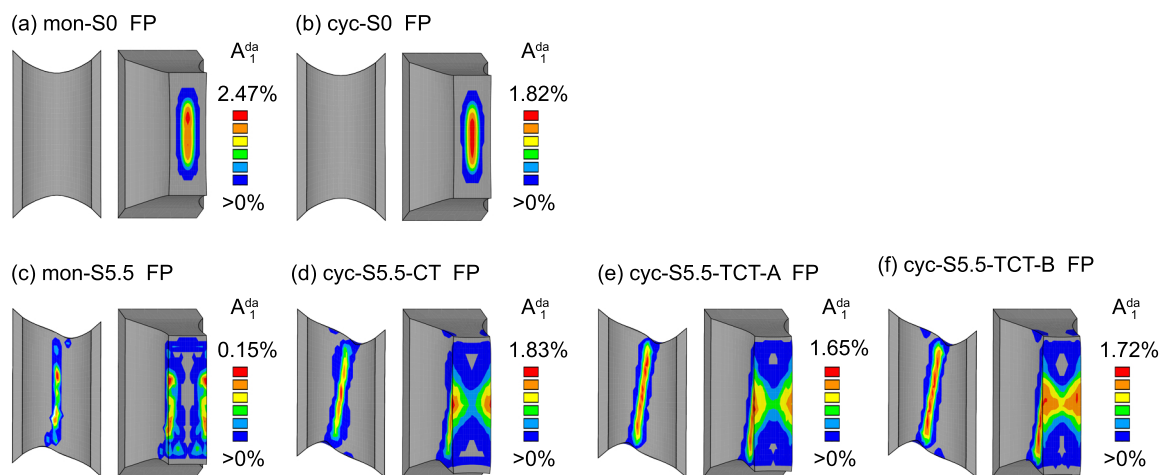
Figure 8. Numerically predicted distribution of the first principal damage strains A_1^{da} on the notch surfaces and notched cross-sections (FP= fracture point).

5.3. Stress Triaxiality, Load Parameter, and Damage Mechanisms

The stress triaxiality

$$\eta = \frac{I_1}{3\sqrt{3J_2}} \tag{13}$$

is widely used to characterize the stress states in numerical analysis, where I_1 and J_2 are stress invariants, respectively. Based on previous studies, the distribution of the stress triaxiality is nearly uniform on the notched cross-section. Thus, the mean stress triaxiality

$$\bar{\eta} = \frac{1}{S} \int_0^S \eta \, ds \tag{14}$$

over the notched cross-section with area S is introduced to provide a more accurate description of the stress state in the experiments. Moreover, the mean stress triaxiality-displacement curves for all investigated experiments are plotted in Figure 9.

As shown in Figure 9a, the mean stress triaxiality $\bar{\eta}$ is around 0.69 during the loading mon-S0. In the cyclic loading test cyc-S0, the mean stress triaxiality $\bar{\eta}$ is 0.69 under tensile loading patterns (before RP1 and RP2-FP), but it becomes negative ($\bar{\eta} = -0.70$) during the compressive loading stage. As pointed out in [12], the damage is caused by the growth of micro-voids under a high stress triaxiality, resulting in fracture behavior. This phenomenon is confirmed by the SEM images in Figure 10a,b, where larger micro-voids are clearly visible. Moreover, jagged fracture lines are observed in Figure 10a,b, which is a characteristic typically associated with a high stress triaxiality.

As illustrated in Figure 9c–f, the mean stress triaxiality $\bar{\eta}$ for the experiments superimposed by 5.5 kN is approximately 0.05 during the preloading stage. It is indicated that the micro-defects are initially deformed in the shear loading direction, forming micro-shear cracks. After the preloading stage, the mean stress triaxialities $\bar{\eta}$ differ under different loading patterns. For example, the $\bar{\eta}$ reaches 0.17 at FP in the mon-S5.5 test, whereas in the cyc-S5.5-CT, cyc-S5.5-TCT-A, and cyc-S5.5-TCT-B experiments, it increases to 0.3, 0.33, and 0.33, respectively. Moreover, the mean stress triaxialities $\bar{\eta}$ are nearly zero under the compressive loading patterns superimposed by 5.5 kN, as seen in Figure 9d–f. Therefore, these findings align with the observations in the SEM pictures shown in Figure 10c–f, where micro-shear cracks are predominant under the mon-S5.5 loading condition, and both micro-shear-cracks and micro-voids are visible in the other cyclic loading experiments. Moreover, the size and depth of the micro-voids are smaller and shallower than those of the ones observed in the mon-S0 and cyc-S0 tests. On the other hand, the fracture lines appear smoother and straighter (see Figure 10c–f) which corresponds to the distributions of the total strain and damage strain; see Figures 6 and 8.
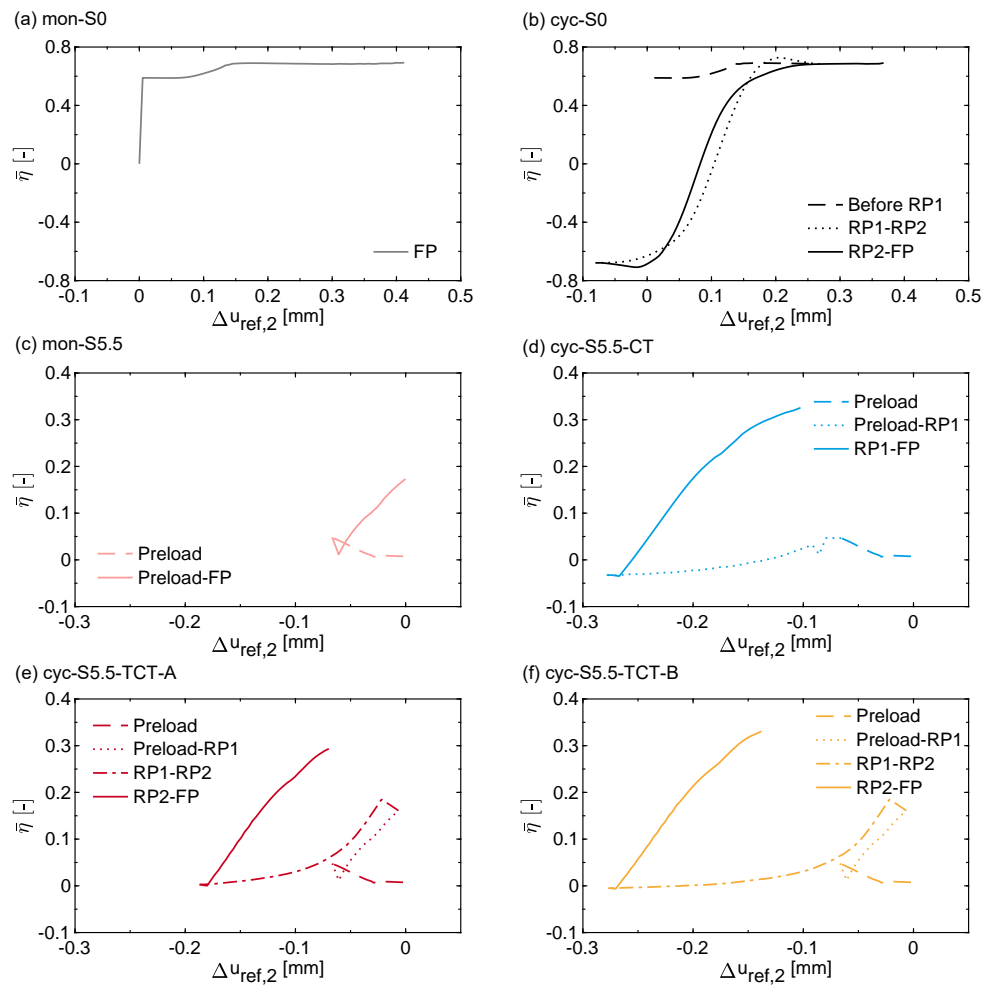
Figure 9. Mean stress triaxiality-displacement curves. RP1, RP2, and FP mean reverse point 1, reverse point 2, and fracture point, respectively. The loading direction changes at each reverse point.
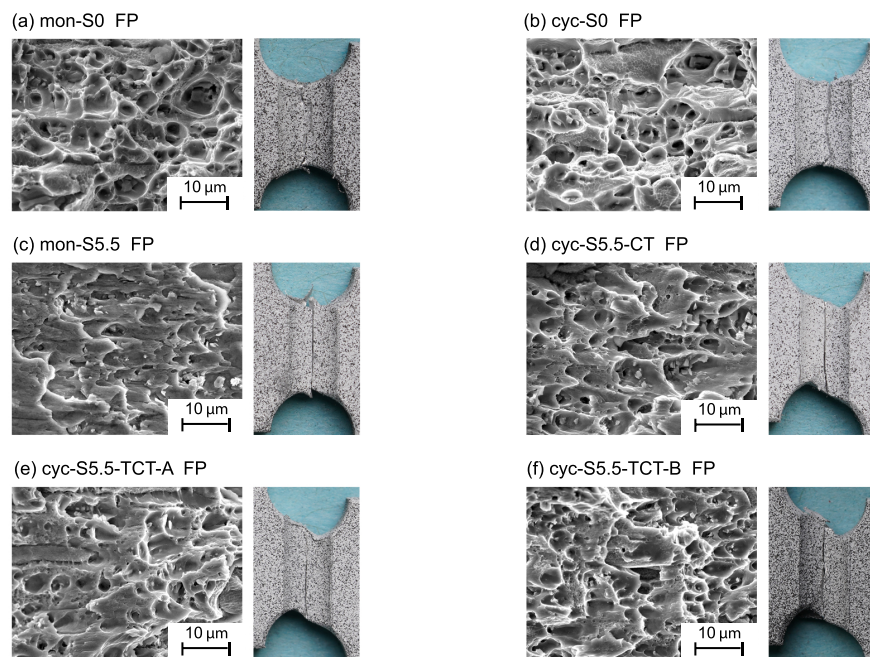

Figure 10. SEM pictures and fracture lines taken from the fracture surfaces.

Additionally, larger or coalesced micro-defects are observed in the cyc-CT loading path compared to the cyc-TCT loading conditions. In the numerical simulations, the predicted damage strain in the cyc-CT test is also larger than in the cyc-S5.5-TCT-A and -B experiments, as presented in Figure 8. One possible reason could be that the micro-defects experience some growth during the first tensile loading pattern in cyc-TCT. Subsequently, they undergo partial closure during the following compressive loading before deforming in the shear direction. In future work, it is recommended to examine the changes of the micro-defects metallographically with micrographs at RP1, RP2, and FP. In conclusion, the experiments successfully generated different stress states, leading to distinct damage mechanisms and fracture behavior, as confirmed by the SEM images. Importantly, ample evidence demonstrates the influence of stress states on damage mechanisms.

6. Conclusions

This study uses an anisotropic elastic–plastic–damage continuum model incorporating combined hardening and softening rules to predict the material mechanical responses under monotonic and cyclic loading conditions. Moreover, the proposed material model has been successfully implemented as a user-defined subroutine in Ansys. The numerical results show good agreement with the experimental ones in both the force-displacement and strain fields. One of the highlights of the present work is that the changes in strain fields during the full loading path can be accurately captured.

The experimental and numerical results confirmed that the loading histories and the preload degree significantly influence the plastic, damage, and fracture behaviors. The experiments superimposed without preloads induce a high stress triaxiality, and the damage is due to the growth of the micro-voids. On the other hand, the tests superimposed by 5.5 kN under monotonic and cyclic loading conditions show quite different damage phenomena. Micro-shear cracks are predominated under both monotonic and cyclic loading, whereas larger and more coalesced micro-defects are exhibited in the cyclic loading patterns.

One significant contribution of this study is confirming the influence of loading histories on the mechanical responses of ductile metals. Moreover, this study introduces a novel set of non-proportional biaxially loaded experiments specifically designed for 4 mm thick metal sheets.

References

1. Gao, X.; Zhang, G.; Roe, C. A study on the effect of the stress state on ductile fracture. *Int. J. Damage Mech.* **2010**, *19*, 75–94.
2. Lou, Y.; Yoon, J.W. Anisotropic yield function based on stress invariants for BCC and FCC metals and its extension to ductile fracture criterion. *Int. J. Plast.* **2018**, *101*, 125–155. [CrossRef]

3. Yue, Z.; Cao, K.; Badreddine, H.; Saanouni, K.; Gao, J. Failure prediction on steel sheet under different loading paths based on fully coupled ductile damage model. *Compos. Sci. Technol.* **2019**, *153–154*, 1–9. [CrossRef]
4. Lou, Y.; Zhang, S.; Yoon, J.W. Strength modeling of sheet metals from shear to plane strain tension. *Int. J. Plast.* **2020**, *134*, 102813. [CrossRef]
5. Xing, L.; Zhan, M.; Gao, P.F.; Li, M.; Dong, Y.D.; He, W.W. The interactive effect of microstructure and stress state on the microscopic damage development of aluminum alloy tailor-welded blank. *Mater. Des.* **2020**, *193*, 108836. [CrossRef]
6. Peng, Z.; Zhao, H.; Li, X. New ductile fracture model for fracture prediction ranging from negative to high stress triaxiality. *Int. J. Plast.* **2021**, *145*, 103057. [CrossRef]
7. Li, H.; Fu, M.W.; Lu, J.; Yang, H. Ductile fracture: Experiments and computations. *Int. J. Plast.* **2011**, *27*, 147–180. [CrossRef]
8. Dunand, M.; Mohr, D. On the predictive capabilities of the shear modified Gurson and the modified Mohr–Coulomb fracture models over a wide range of stress triaxialities and Lode angles. *J. Mech. Phys. Solids* **2011**, *59*, 1374–1394. [CrossRef]
9. Voyiadjis, G.Z.; Hoseini, S.H.; Farrahi, G.H. A Plasticity Model for Metals With Dependency on All the Stress Invariants. *J. Eng. Mater. Technol.* **2013**, *135*, 011002. [CrossRef]
10. Roth, C.C.; Morgeneyer, T.F.; Cheng, Y.; Helfen, L.; Mohr, D. Ductile damage mechanism under shear-dominated loading: In-situ tomography experiments on dual phase steel and localization analysis. *Int. J. Plast.* **2018**, *109*, 169–192. [CrossRef]
11. Peng, J.; Wang, Y.; Dai, Q.; Liu, X.; Liu, L.; Zhang, Z. Effect of Stress Triaxiality on Plastic Damage Evolution and Failure Mode for 316L Notched Specimen. *Metals* **2019**, *9*, 1067. [CrossRef]
12. Wei, Z.; Zistl, M.; Gerke, S.; Brünig, M. Analysis of ductile damage and fracture under reverse loading. *Int. J. Mech. Sci.* **2022**, *228*, 107476. [CrossRef]
13. Kong, X.; Chen, J.; Madi, Y.; Missoum-Benziane, D.; Besson, J.; Morgeneyer, T. Plasticity and ductility of an anisotropic recrystallized AA2198 Al-Cu-Li alloy in T3 and T8 conditions during proportional and non-proportional loading paths: Simulations and experiments. *J. Theor. Appl. Mech.* **2023**. [CrossRef]
14. Pirondi, A.; Bonora, N.; Steglich, D.; Brocks, W.; Hellmann, D. Simulation of failure under cyclic plastic loading by damage models. *Int. J. Plast.* **2006**, *22*, 2146–2170. [CrossRef]
15. Kanvinde, A.M.; Deierlein, G.G. Cyclic Void Growth Model to Assess Ductile Fracture Initiation in Structural Steels due to Ultra Low Cycle Fatigue. *J. Eng. Mech.* **2007**, *133*, 701–712. [CrossRef]
16. Voyiadjis, G.Z.; Hoseini, S.H.; Farrahi, G.H. Effects of stress invariants and reverse loading on ductile fracture initiation. *Int. J. Solids Struct.* **2012**, *49*, 1541–1556. [CrossRef]
17. Algarni, M.; Bai, Y.; Zwawi, M.; Ghazali, S. Damage evolution due to extremely low-cycle fatigue for Inconel 718 alloy. *Metals* **2019**, *9*, 1109. [CrossRef]
18. Papasidero, J.; Doquet, V.; Mohr, D. Ductile fracture of aluminum 2024-T351 under proportional and non-proportional multi-axial loading: Bao–Wierzbicki results revisited. *Int. J. Solids Struct.* **2015**, *69–70*, 459–474. [CrossRef]
19. Cortese, L.; Nalli, F.; Rossi, M. A nonlinear model for ductile damage accumulation under multiaxial non-proportional loading conditions. *Int. J. Plast.* **2016**, *85*, 77–92. [CrossRef]
20. Raj, A.; Verma, R.K.; Singh, P.K.; Shamshoddin, S.; Biswas, P.; Narasimhan, K. Experimental and numerical investigation of differential hardening of cold rolled steel sheet under non-proportional loading using biaxial tensile test. *Int. J. Plast.* **2022**, *154*, 103297. [CrossRef]
21. Kong, X.; Morgeneyer, T.F.; Missoum-Benziane, D.; Rousselier, G. A polycrystalline damage model applied to an anisotropic aluminum alloy 2198 under non-proportional load path changes. *Int. J. Plast.* **2023**, *168*, 103674. [CrossRef]
22. Wei, Z.; Gerke, S.; Brünig, M. Damage and fracture behavior under non-proportional biaxial reverse loading in ductile metals: Experiments and material modeling. *Int. J. Plast.* **2023**, *171*, 103774. [CrossRef]
23. Wei, Z.; Gerke, S.; Brünig, M. Numerical analysis of non-proportional biaxial reverse experiments with a two-surface anisotropic cyclic plasticity-damage approach. *Comput. Methods Appl. Mech. Eng.* **2024**, *419*, 116630. [CrossRef]
24. Yoshida, F.; Uemori, T.; Fujiwara, K. Elastic–plastic behavior of steel sheets under in-plane cyclic tension–compression at large strain. *Int. J. Plast.* **2002**, *18*, 633–659. [CrossRef]
25. Cao, J.; Lee, W.; Cheng, H.S.; Seniw, M.; Wang, H.P.; Chung, K. Experimental and numerical investigation of combined isotropic-kinematic hardening behavior of sheet metals. *Int. J. Plast.* **2009**, *25*, 942–972. [CrossRef]
26. Gurson, A.L. Continuum theory of ductile rupture by void nucleation and growth: Part I—Yield criteria and flow rules for porous ductile media. *J. Eng. Mater. Technol.* **1977**, *99*, 2–15. [CrossRef]
27. Tvergaard, V.; Needleman, A. Analysis of the cup-cone fracture in a round tensile bar. *Acta Metall.* **1984**, *32*, 157–169. [CrossRef]
28. Tvergaard, V. Material failure by void growth to coalescence. *Adv. Appl. Mech.* **1989**, *27*, 83–151.
29. Nahshon, K.; Hutchinson, J.W. Modification of the Gurson model for shear failure. *Eur. J. Mech. A Solids* **2008**, *27*, 1–17. [CrossRef]
30. Malcher, L.; Andrade Pires, F.M.; César de Sá, J. An extended GTN model for ductile fracture under high and low stress triaxiality. *Int. J. Plast.* **2014**, *54*, 193–228. [CrossRef]
31. Morin, L.; Leblond, J.B.; Mohr, D.; Kondo, D. Prediction of shear-dominated ductile fracture in a butterfly specimen using a model of plastic porous solids including void shape effects. *Eur. J. Mech. A Solids* **2017**, *61*, 433–442. [CrossRef]
32. Khan, I.A.; Benzerga, A.A.; Needleman, A. A shear modified enhanced Gurson constitutive relation and implications for localization. *J. Mech. Phys. Solids* **2023**, *171*, 105153. [CrossRef]

33. Simo, J.C.; Ju, J.W. Strain- and stress-based continuum damage models—I. Formulation. *Int. J. Solids Struct.* **1987**, *23*, 821–840. [CrossRef]

34. Voyiadjis, G.Z.; Kattan, P.I. *Advances in Damage Mechanics: Metals and Metal Matrix Composites*; Elsevier: Amsterdam, The Netherlands, 1999.

35. Brünig, M. An anisotropic ductile damage model based on irreversible thermodynamics. *Int. J. Plast.* **2003**, *19*, 1679–1713. [CrossRef]

36. Voyiadjis, G.Z.; Kattan, P.I. *Damage Mechanics*; CRC Press: Boca Raton, FL, USA, 2005.

37. Murakami, S. *Continuum Damage Mechanics*; Springer: Dordrecht, The Netherlands, 2012; Volume 185.

38. Vignjevic, R.; Djordjevic, N.; Panov, V. Modelling of dynamic behaviour of orthotropic metals including damage and failure. *Int. J. Plast.* **2012**, *38*, 47–85. [CrossRef]

39. Balieu, R.; Kringos, N. A new thermodynamical framework for finite strain multiplicative elastoplasticity coupled to anisotropic damage. *Int. J. Plast.* **2015**, *70*, 126–150. [CrossRef]

40. Badreddine, H.; Saanouni, K. On the full coupling of plastic anisotropy and anisotropic ductile damage under finite strains. *Int. J. Damage Mech.* **2017**, *26*, 1080–1123. [CrossRef]

41. Brünig, M.; Gerke, S.; Hagenbrock, V. Micro-mechanical studies on the effect of the stress triaxiality and the Lode parameter on ductile damage. *Int. J. Plast.* **2013**, *50*, 49–65. [CrossRef]

42. Spitzig, W.A.; Richmond, O. The effect of pressure on the flow stress of metals. *Acta Metall.* **1984**, *32*, 457–463. [CrossRef]

43. Holmen, J.K.; Frodal, B.H.; Hopperstad, O.S.; Børvik, T. Strength differential effect in age hardened aluminum alloys. *Int. J. Plast.* **2017**, *99*, 144–161. [CrossRef]

44. Zhang, J.; Brepols, T.; Reese, S. A two–surface damage–plasticity model based on a Drucker—Prager yield criterion. *Proc. Appl. Math. Mech.* **2023**, *22*, e202200296. [CrossRef]

45. Chaboche, J.L.; Rousselier, G. On the Plastic and Viscoplastic Constitutive Equations—Part I: Rules Developed With Internal Variable Concept. *J. Press. Vessel Technol.* **1983**, *105*, 153–158. [CrossRef]